optics

MDPI

Article

Photomechanical Sensing from Spectral Shifts in Graphene-Doped Polydimethylsiloxane Reflection Gratings

Abigail Deaton, Hengzhou Liu and Nathan J. Dawson *

Department of Physics, Florida Polytechnic University, Lakeland, FL 33805, USA
* Correspondence: ndawson@floridapoly.com

Abstract

Polydimethylsiloxane (PDMS) films doped with graphene nanoplatelets (GNP) with an embossed surface-relief grating were investigated as photothermal actuated sensors. The films were initially characterized using controlled environmental heating where the wavelength of a diffracted white-light probe beam measured at a fixed angle increased monotonically with temperature due to thermal expansion of the grating. An asymmetric double sigmoidal function tracked the shift in peak diffraction wavelength. The observed thermal response is consistent with the thermal expansion of a freestanding PDMS composite film. When a continuous-wave (CW) laser was incident on the film, intensity-dependent photothermal expansion caused a transient deformation in the grating. The photomechanical behavior of the grating, tracked by the diffracted probe beam with a miniature spectrometer, was then shown to act as a laser power meter. These results demonstrate that photomechanical materials can be used as add-ons to existing optical spectroscopy devices for power-sensing applications.

Keywords: photomechanical; graphene nanoplatelets; polydimethylsiloxane; diffraction grating; optical spectroscopy; thermal expansion; photothermal heating

1. Introduction

Optical power is most commonly measured by converting absorbed light into an electrical signal. For continuous-wave (CW) laser measurements, the most common devices are either based on photodiodes [1–3] or thermocouples [4–6]. Photodiode-based sensors offer direct conversion of absorbed light into electrical current, but their operational wavelength range is constrained by the semiconductor bandgap [7,8]. Although their responsivity must be calibrated as a function of photon energy, photodiodes offer high sensitivity and fast response times [8–10]. Thermopile detectors offer a different method to measure incident optical power by converting absorbed radiation into heat and then into a measurable voltage per the Seebeck effect [11–13]. These detectors often have coatings that allow for a broadband spectral response that can be calibrated with respect to the incident wavelength [14,15]. Thermopile detectors are well suited for measuring moderate to high optical powers; however, their response times are typically much slower than those of photodiodes [12,16–18]. In this article, we present a CW laser intensity detector that converts the pump light to heat in an elastomeric film doped with graphene nanoplatelets (GNP). The dopant GNP have a broad absorbance profile through the visible spectrum to the mid infrared. The increase in temperature is not measured by thermocouples in the presented device, but rather from the thermally-driven photomechanical motion of the film via a diffraction grating embossed on one surface. A similar power measurement

Academic Editor: Patrick Görrn

Received: 2 March 2026
Revised: 20 March 2026
Accepted: 25 March 2026
Published: 27 March 2026

device was created by Sun et al. [19], but it relied on a monochromatic probe beam that passed through the film to be diffracted on a linear CCD array. Here, we present a method that uses a low-power probe beam of white light incident on a reflection grating, and the diffracted beam is sensed by a fixed-position fiber spectrometer. Photomechanical actuation is shown to change the grating spacing, which in turn changes the color of light incident on the fiber interface.

A reversible photomechanical effect has been observed in many materials [20,21]; however, there are only a few physical mechanisms responsible for actuation. In piezoelectric materials, light can induce charge redistribution that produces strain via the inverse piezoelectric effect [22,23]. Uchino showed that stacking piezoelectric ceramics increases the photostrictive response and results in greater mechanical displacement [24], which was instrumental in realizing the Uchino walker [25,26]. Large macroscopic photomechanical deformations have been observed from microscopic changes to molecular structure such as the photoisomerization of azo moieties [27,28]. Several polymers have been engineered to contain either side-chain or end-chain azo groups [29–32]. Photomechanical effects have also been report in polymers doped with azobenzene derivatives [33,34]. Liquid crystal elastomers (LCEs) containing azobenzene derivatives also show great promise as photomechanical materials [35–39], where large contractions along the director have been reported in pre-strained films [40]. In some experimental configurations, photothermal heating was found to be the dominant mechanism for photomechanical actuation of LCEs [41–44].

Because photothermal heating can dominate the response of a photomechanical material, many studies have focused on elastomeric materials that have large coefficients of thermal expansion such as polydimethylsiloxane (PDMS) [45–47]. Unless a transmission window is required for the application, photomechanical materials based on PDMS are typically doped with conjugated carbon networks such as graphene or nanotubes due to the high photothermal conversion efficiency [48–51]. As opposed to the work by Sun et al. [19], our measurements rely on a reflective grating geometry for sensing, which allows for GNP doping of the PDMS material.

2. Materials and Methods

Samples of GNP-PDMS were prepared with Sylgard 184 (Dow Corning, Midland, MI, USA) mixed at a 10:1 ratio of base to curing agent by weight. A 5 mL volume of PDMS base was first dispensed into a 20 mL glass vial. The GNP powder was then added and homogenized with the base. The doped base was then mixed with the curing agent until the mixture reached the proper consistency. Mixing introduced air bubbles, where each final mixture was dessicated for over 20 min to remove the bubbles. The dessicated mixtures were then poured onto a polycarbonate diffraction grating mold. The grating mold was obtained by mechanically splitting a DVD to expose the grating layer, which was cleaned with ethanol and allowed to dry. Spacers were introduced on both sides of the pre-cured puddle and a blade was run over the top of the liquid to create a uniform layer above the grating surface. The liquid samples were each crosslinked into single elastomeric materials by placing them in an oven at 80 °C for two hours. The process of fabricating the grating-embossed GNP-PDMS films is illustrated in Figure 1a. After curing, the elastomeric films were peeled from the mold and inspected. The resultant GNP-PDMS film was doped with 0.3 wt.% nanoplatelets and ∼800 µm thick. Individual samples were trimmed into rectangular sections, with the longer dimension used for mounting and alignment in the experimental apparatus.

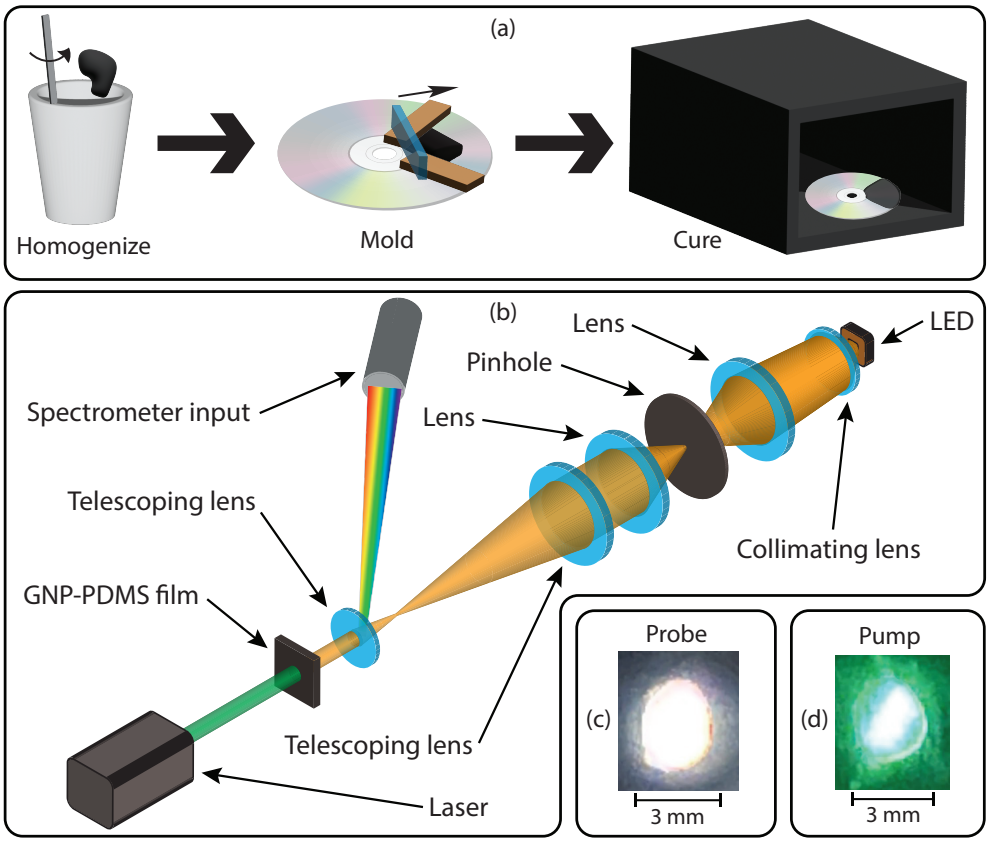

Figure 1. (**a**) An illustration of the GNP-PDMS fabrication steps. (**b**) Experimental setup used for both temperature-controlled and pump-laser measurements. The probe beam, optical filtering elements, and spectrometer geometry remained fixed across each series of experiments. Images of the (**c**) probe and (**d**) pump beam profiles.

To investigate whether a GNP-doped PDMS diffraction grating can be used to estimate the power of a CW laser through spectral shifts caused by photothermal heating, we conducted two separate experiments. For temperature-controlled measurements, the PDMS grating was enclosed within a rectangular acrylic chamber to create a thermally insulated environment. A thermistor was positioned near the sample surface to monitor temperature, while DC ceramic heaters controlled the internal temperature. The temperature inside the chamber was swept from 30 °C to 80 °C. The sample was heated uniformly while the probe beam continuously illuminated the grating.

The optical configuration used to probe the diffraction response was identical for both the temperature-controlled and laser-heating experiments. A spectrally flat, white LED (Seoul Semiconductor S1S0-3030509506-0000003S-00001, Seoul Semiconductor, Ansan, Republic of Korea) [52] was passed through a 0.3 numerical aperture (NA) collimating lens (Edmund Optics, Barrington, NJ, USA). The probe beam was then spatially filtered using a pinhole to improve beam quality and then finely collimated by additional lenses as shown in Figure 1b. The white light beam diameter incident on the surface of the film was estimated from the image shown in Figure 1c. A 200 µm multimode fiber at a fixed position and orientation was fed into an Ocean Optics USB 4000 spectrometer (Ocean Optics, Inc., Dunedin, FL, USA) to track the spectrum of the diffracted probe beam. The input end of the fiber was directed towards the probe beam and located ∼8 cm from the film. During the temperature dependent measurements, the fiber end was ∼62° from the norm of the film grating. The angle gives an estimated period of the embossed GNP-PDMS grating of ∼700 nm for a peak wavelength measured to be ∼616 nm after extrapolating experimental data to 25 °C.

A continuous-wave (CW) laser diode was used for the pump-probe experiment illustrated in Figure 1a with the profile imaged in Figure 1d. A KG-1 Schott glass filter (Edmund Optics, Barrington, NJ, USA) was used to remove the residual 1064 nm light from the beam. Prior to data collection, both pump and probe sources were allowed to reach stable output conditions. The pump beam illuminated the GNP-PDMS film on the opposite side of the grating.

3. Results

3.1. Uniform Heating

The GNP-PDMS grating film was first evaluated under controlled heating to determine how the spectral peak and line shape changed with temperature. The finite probe beam diameter and heterogeneous defects in the grating resulted in a spectral profile with some asymmetry. Therefore, the diffraction spectrum at each temperature was fitted using an asymmetric double sigmoid,

$$I(\lambda) = \frac{A}{1+f_1(\lambda)}\left[1 - \frac{1}{1+f_2(\lambda)}\right], \tag{1}$$

where A is the amplitude and

$$f_j(\lambda) = \exp\left(\frac{\lambda_0 - \lambda + (-1)^j w/2}{s_j}\right). \tag{2}$$

In Equation (2), λ_0 is the peak wavelength, w is related to the broadness of the peak, and the s_j parameters adjust the steepness of the short- and long-wavelength edges.

Prior to fitting, electronic drift was corrected by averaging 100 data points in the infrared spectrum and subtracting it from the spectrum. All experimental spectra are normalized by dividing them by their individual peak values determined from initial fits. The recorded spectra for a few temperatures is shown in Figure 2a along with the best fit lines for each spectra shown. For first-order diffraction ($m = 1$) under near-normal incidence of an infinitesimal beam spot, the grating equation for the peak wavelength reduces to

$$\lambda = a \sin\theta \qquad (\text{for } m = 1), \tag{3}$$

where λ is the peak wavelength of the diffracted beam and θ is the diffraction angle. Because the measurement geometry fixes θ, changes in λ are associated with changes in the grating spacing a. The observed increase in wavelength with temperature is therefore directly proportional to the increase in the grating period caused by thermal expansion of the GNP-PDMS matrix.

The peak wavelength λ_0 is plotted as a function of temperature in Figure 2b. A linear best fit line is also shown in Figure 2b with a slope of (1.41 ± 0.05) Å $^\circ$C^{-1}. This linear trend is consistent with both the proportionality relationship of a and λ for fixed θ in Equation (3) and also the first-order, linear thermal expansion approximation,

$$\frac{\Delta a}{a_0} = \alpha(T - T_0). \tag{4}$$

In Equation (4), a_0 is the initial grating spacing at temperature T_0 and α is the coefficient of linear thermal expansion for the GNP-PDMS film. The slope of the peak wavelength as a

function of temperature plot and the initial peak wavelength at 25 °C can determine the coefficient of linear thermal expansion,

$$\alpha = \frac{1}{\lambda_0}\left(\frac{d\lambda}{dT}\right). \tag{5}$$

For an extrapolated peak wavelength of 616.6 nm at 25 °C, straightforward calculation yields $\alpha = (2.29 \pm 0.08) \times 10^{-4}\ ^{\circ}\mathrm{C}^{-1}$. The value determined with this method for Sylgard 184 doped with 0.3 wt.% GNPs is ∼75 % of the value for pure Sylgard 184 given by Müller et al. [53].

Additional parameters obtained from fitting the temperature-dependent diffraction spectra are shown in Figure 2c. In contrast to the monotonic redshift of the peak wavelength with increasing temperatures, the spectral width and steepness parameters exhibit a nonlinear temperature dependence. These parameters were approximately constant up to 50 °C, above which the width parameter w increased while the steepness parameters s_j decreased. Here, an increase in w corresponds to a broadening of the spectral peak, whereas smaller values of s_j produce steeper spectral edges. Although the overall peak width remained nearly unchanged, spectral features became less sharply defined at higher temperatures which indicates a redistribution of the spectral intensity profile as opposed to a simple narrowing or broadening.

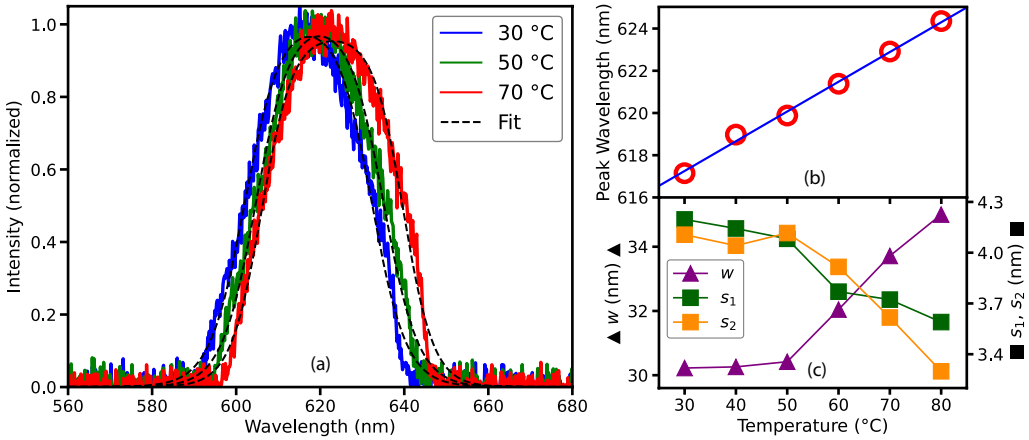

Figure 2. (**a**) Recorded spectra (solid) for the first-order diffracted beam at select temperatures along with the corresponding asymmetric double sigmoidal fits (dashed). (**b**) The peak wavelength as a function of temperature. (**c**) The w, s_1, and s_2 fit parameters as a function of temperature.

3.2. Laser Heating

The diffraction response of the GNP-PDMS grating under direct laser illumination was investigated using a pump-probe geometry. As described in Section 2, a CW pump laser was incident on the back side of the film and absorbed by the GNPs, while a ∼150 mW white-light probe beam continuously interrogated the embossed grating surface. Figure 3 shows a contour plot of the diffracted probe spectrum as a function of time when the pump power of the diode laser was 97.5 mW. After opening the shutter at $t = 0$, a sharp redshift of the diffracted beam's peak is observed. The peak reversibly returns to the initial peak wavelength after the shutter is closed. The spectral evolution is continuous in time which shows that the dominant effect of laser illumination is a smooth photothermal expansion of the grating in response to a step in incident power.

The peak wavelength was extracted from asymmetric double-sigmoid fits to quantify the transient behavior for various pump powers. Figure 4a shows the recorded spectra for the diffracted beam immediately after the shutter was opened, and it continues to show the response after the shutter was closed. For the full range of pump powers studied, the peak

wavelength increased monotonically after the shutter was opened. The magnitude and rate of the shift increased with incident optical power. After the shutter was closed, the peak wavelength relaxed back toward its initial value on a comparable timescale.

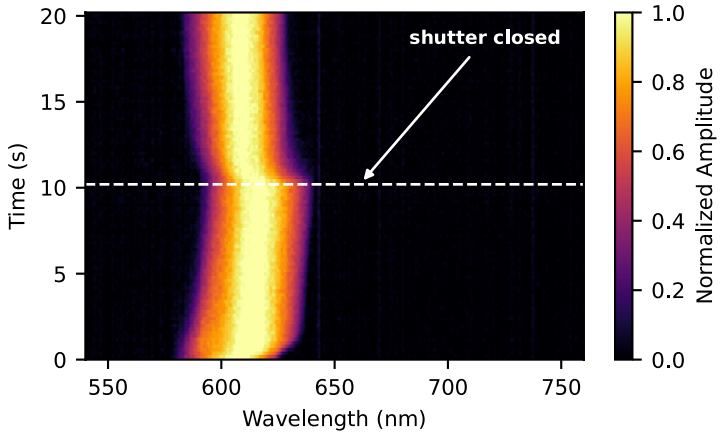

Figure 3. A contour plot of the normalized spectra as a function of time for an incident pump beam with a power of 97.5 mW.

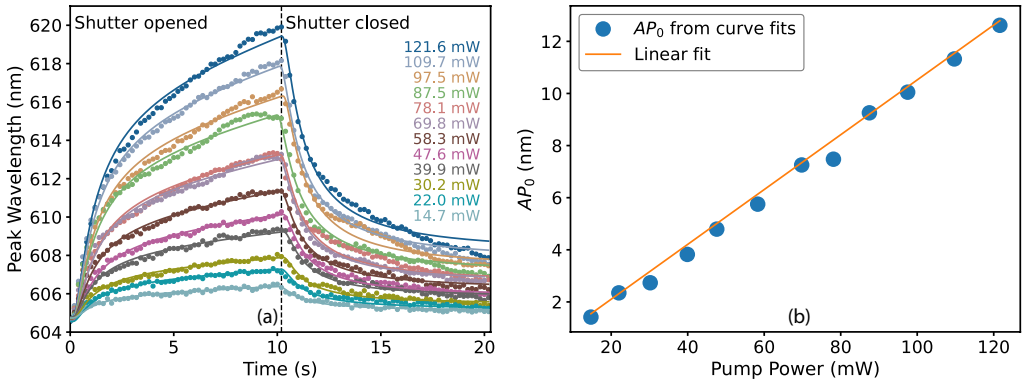

Figure 4. (**a**) Peak wavelength as a function of time subject to a shuttered pump beam. (**b**) The fitted parameter AP_0 as a function of the measured pump power P_0.

The transient peak wavelength data were modeled to account for the spatially distributed pump absorption and surface probe sensing. The local photothermal expansion at a point within the film is governed by the convolution of the absorbed optical power with the local temperature at the probe beam based on the diffusive heat kernel function. Because both the pump beam and probe beam have finite beam sizes incident on the thin film, the experimentally measured response should be spatial convolution of the local expansion at the probe beam which is caused by the pump beam's profile. Therefore, we can estimate the wavelength shift from

$$\lambda(t) = \lambda_0 + \iint Y(\vec{x}, \vec{x}') \int_0^t I(\vec{x}', t') K(\vec{x} - \vec{x}', t - t')\, dt' d\vec{x}' d\vec{x}, \tag{6}$$

where $I(\vec{x}', t')$ is the pump intensity and $Y(\vec{x}, \vec{x}')$ represents the weighting function of the pump and probe beams. The heat kernel is of the standard form,

$$K(\vec{x} - \vec{x}', t - t') = \frac{1}{[4\pi D(t - t')]^{n/2}} e^{-(\vec{x} - \vec{x}')^2 / 4D(t - t')}, \tag{7}$$

where n is the number of dimensions and D is the thermal diffusivity of the film.

After spatial integration of Equation (6), the resultant wavelength response is modeled by way of a time-domain response function obtained after spatial integration,

$$\lambda(t) = \lambda_0 + \int_0^t P(t')G(t-t')\,dt'\,. \tag{8}$$

Experimentally, the time-dependent pump power $P(t)$ was externally shuttered on at $t = 0$ and then off at some t_{off}. The behavior can be modeled with two step functions,

$$P(t) = P_0 H(t) - P_0 H(t - t_{\text{off}})\,, \tag{9}$$

where P_0 is the pump power incident on the film when the shutter is open. The exact analytical form for the Green's function can not be written because of the presence of $Y(\vec{x}, \vec{x}')$ in Equation (6). Based on the form of the heat kernel and the pump power, however, the wavelength as a function of time will be of the form

$$\lambda(t) = \lambda_0 + AP_0\Big\{H(t)\,[1+f(t)]e^{-q/t} - H(t-t_{\text{off}})\,[1+f(t-t_{\text{off}})]e^{-q/(t-t_{\text{off}})}\Big\}\,, \tag{10}$$

where A is the amplitude of the wavelength shift, q is a parameter that depends on the beam weighting and thermal diffusivity, and sets the characteristic short-time diffusion scale of the response, and $f(t)$ is a function of time that captures the complexity of the problem through the dimensionality and overlap. In a previous study with a different beam geometry, Sun et al. arrived at a similar result for a different pump-probe overlap where they assumed $f(t) \sim 0$ [19]. Fits to the experimental data were poor when making the same assumption here; however, for the relatively short pump durations used in this work (∼10 s), the response function can be expanded in a power series and truncated at first order. Under this approximation, $f(t) \approx ct$, where c is a constant, and the wavelength response can then be written in the form

$$\lambda(t) = \lambda_0 + AP_0\Big\{H(t)\,(1+ct)e^{-q/t} - H(t-t_{\text{off}})\,[1+c(t-t_{\text{off}})]e^{-q/(t-t_{\text{off}})}\Big\}\,. \tag{11}$$

Fitting all pump powers simultaneously, c and q were treated as global fit parameters, common to all data sets. For each individual measurement, the product AP_0 was treated as a free parameter, while the pump power P_0 was independently measured using an Ophir PD300-UV power meter (North Logan, UT, USA). The fitted values for AP_0 were subsequently plotted as a function of the measured pump power as shown in Figure 4b. Linear regression yielded $A = (0.105 \pm 0.002)$ nm/mW, which demonstrated a proportional relationship between the incident optical power and the shift in peak wavelength of the measured diffracted probe beam. This two-step procedure allows the linearity of the photothermal response to be directly visualized rather than imposed through a global constraint during fitting. The t_{off} parameter was also fit to individual data runs to capture small differences in shutter timing, but the variation between individual t_{off} values was much less than the 200 ms time step between the recorded spectral measurements. The fits reproduced the observed transient behavior for all pump powers, as shown in Figure 4a.

The global parameters obtained from the simultaneous fit to all of the laser heating data were $c = (2.70 \pm 0.03) \times 10^{-2}$ s^{-1} and $q = (0.946 \pm 0.011)$ s. The agreement between the model and the experimental data confirms that the kernel function captures the essential physics of the pump-induced thermal expansion, including the integrated spatial weighting and transient diffusion. There is a small discrepancy between the model and the experiment at long decay times for higher pump power measurements. The low uncertainty of global fit parameters and visual look of the fitted lines in Figure 1a indicate a consistent photothermal response across all experiments for a static macroscopic geometry.

4. Discussion

The temperature-dependent diffraction measurements established a direct relationship between substrate temperature and the wavelength shift of the embossed surface grating. Because the diffracted probe beam only sampled the surface relief grating period, these measurements confirm that bulk thermal expansion of the substrate is efficiently transferred to the surface structure without evidence of slippage or localized relaxation. The linearity of the wavelength shift over the temperature range tested confirms the use of the grating's temperature response as a quantitative thermometer for soft materials.

The extracted linear thermal expansion coefficient is lower than commonly reported values for pristine Sylgard 184, which suggests that incorporation of graphene nanoplatelets modifies the effective thermo-mechanical properties of the elastomer. While the nanoplatelets enhance optical absorption and heat dissipation, they also introduce mechanical constraints that suppresses macroscopic expansion. This behavior is consistent with composites in general which confirms the need to independently characterizing the static thermal response prior to analyzing the pump-driven transient behavior.

The time-resolved, pump-probe measurements studied the photomechanical effect in the GNP-PDMS film which is essentially a photodriven version of the same thermoelastic mechanism. The global fit parameters c and q describe the transient evolution toward the film reaching a steady-state temperature whereas the fitted amplitude AP_0 directly measures the absorbed optical power in terms of the grating's expansion. The agreement between the static temperature calibration and the photothermal response confirms that the observed dynamics stem from bulk heating rather than nonthermal photomechanical effects. The linear relationship between the fitted amplitude AP_0 and the independently measured pump power P_0 demonstrates that the grating-based photothermal response can be used for optical power metrology. The range over which this linear relationship extends is directly related to the range over which the thermal expansion can be approximated as linear with temperature. Saturable absorption can occur for extremely high intensities which could result in a nonlinear relationship; however, the GNP-PDMS film will also eventually reach a burn threshold at high intensities.

Only the early-time transient response is required to estimate the pump power for a step-function excitation which eliminates the need to wait for full thermal equilibration. Baseline correction and asymmetric double sigmoid fits can be performed rapidly with fit parameters appearing before the next acquisition in time. The quick power measurements are useful from an applications perspective, where the full on/off cycle was only necessary to improve the accuracy of calibration constants.

Choosing PDMS as a substrate material has several practical advantages. The material is low cost and allows for simple embossing techniques to create surface gratings. As demonstrated, the measurement method can be implemented as an add-on to miniature spectrometers that are commonly found in optics laboratories. The demonstrated operation at typical levels of diode laser power further highlights the relevance of the technique for routine laboratory use. Furthermore, the incorporation of graphene nanoplatelets results in broadband optical absorption across the visible and near-infrared spectral range which allows for power measurements of lasers with differing wavelengths using a single device geometry.

Several limitations of the present implementation also suggest clear pathways for improvement. Because the asymptotic behavior of the thermal response occurs at long times, the current approach requires a well-defined duration of exposure to the pump to accurately measure the optical power. Also, a small fraction of the pump light can transmit through the film even at relatively high optical densities, which can introduce systematic errors in power estimation. Moreover, the sensitivity of the response is fundamentally

limited by the thermal expansion coefficient of PDMS, which constrains the minimum detectable power for continuous-wave excitation. The spatial weighting function $Y(\vec{x}, \vec{x}')$ also introduces variability and sensitivity to the pump beam spot size and position on the sample.

There are some possible improvements that can be made in terms of an laser power meter based on the limitations we just described. For example, reducing the film thickness or coupling the substrate to a thermally conductive heat sink would shorten the time required for the peak wavelength to asymptotically approach the full shift in wavelength. To mitigate pump light leakage into the spectrometer, an ultrathin reflective coating (e.g., aluminum) could be deposited on the grating surface to reflect residual pump light back into the absorbing composite and simultaneously enhance the probe beam diffraction efficiency. The sensitivity to low laser powers could be enhanced by replacing PDMS with a material that has a larger photomechanical response such as a prestrained liquid crystal elastomer which would allow for a large contraction along the director under photothermal heating. Furthermore, the broadness of spectra recorded by the spectrometer is determined by the probe beam spot size and distance between the diffraction grating and spectrometer interface. Therefore, reducing the size of the probe beam or increasing the distance between the diffraction grating and the spectrometer will result in a narrower spectral profile. Last, creating an aperture that only allows commonly sized laser beams through would lower the uncertainty in the incident beam's placement on the film and reduce sensitivity to spatial nonuniformities and allow for practical power-meter implementations.

5. Conclusions

We demonstrated that a GNP-doped PDMS film embossed with a surface diffraction grating provides a quantitative measure of photothermal expansion via a diffracted white-light probe beam diffracted onto a spectrometer's input. Temperature-dependent diffraction measurements established a linear relationship between substrate temperature and the grating period to determine, in general, the linear thermal expansion coefficient for soft material. The reduced expansion coefficient of GNP-PDMS relative to pristine Sylgard 184 reveals how nanoplatelet doping modifies the thermo-mechanical response.

Time-resolved pump-probe measurements showed a reversible photothermal response through diffusive heat transport and spatial beam overlap. A convolution-based model with a small set of physically motivated parameters accurately reproduced the transient wavelength shifts across the range of pump powers tested. The fitted amplitude of the response scaled linearly with the independently measured pump power, which illustrates how the diffracted probe's spectrum yields a direct optical signature of absorbed power.

These results establish a foundation for creating a simple, broadband optical power measurement apparatus based on photothermal deformation of soft materials. The use of elastomers and broadband absorbers makes the technique a low-cost option for power measurements when also utilizing a portable laboratory spectrometer. While limitations related to thermal time constants, optical leakage, and material sensitivity remain, we have identified specific improvements that allow for grating-based photothermal metrology in future implementations.

Author Contributions: Conceptualization, N.J.D.; Methodology, A.D. and N.J.D.; Validation, A.D. and N.J.D.; Formal analysis, A.D. and N.J.D.; Investigation, A.D. and N.J.D.; Data curation, N.J.D.; Writing—original draft, A.D. and N.J.D.; Writing—review and editing, H.L. and N.J.D.; Visualization, H.L. and N.J.D.; Supervision, H.L. and N.J.D.; Project administration, N.J.D.; Funding acquisition, N.J.D. All authors have read and agreed to the published version of the manuscript.

Funding: This material is based upon work supported by the National Science Foundation (Grant No. 2337595).

Data Availability Statement: The data presented in this study are openly available in Zenodo at https://doi.org/10.5281/zenodo.18829952, accessed on 2 March 2026.

Conflicts of Interest: The authors declare no conflicts of interest.

References

1. Envall, J.; Kärhä, P.; Ikonen, E. Measurements of fibre optic power using photodiodes with and without an integrating sphere. *Metrologia* **2004**, *41*, 353. [CrossRef]
2. Krishnan, S.; Bindra, K.S.; Oak, S.M. A sensitive and high dynamic range cw laser power meter. *Rev. Sci. Instrum.* **2008**, *79*, 125101. [CrossRef]
3. Pecunia, V.; Anthopoulos, T.D.; Armin, A.; Bouthinon, B.; Caironi, M.; Castellanos-Gomez, A.; Chen, Y.; Cho, K.; Clegg, C.; Fang, X.; et al. Guidelines for accurate evaluation of photodetectors based on emerging semiconductor technologies. *Nat. Photon.* **2025**, *19*, 1178–1188. [CrossRef]
4. Khomenko, A.; García-Weidner, A.; Tapia-Mercado, J.; García-Zárate, M. High-resolution fast response fiber-optic laser calorimeter using a twin interferometric temperature sensor. *Opt. Commun.* **2001**, *198*, 29–35. [CrossRef]
5. St-Antoine, B.C.; Ménard, D.; Martel, R. Single-Walled Carbon Nanotube Thermopile for Broadband Light Detection. *Nano Lett.* **2011**, *11*, 609–613. [CrossRef] [PubMed]
6. Piotrowska, A.K.; Łaszcz, A.; Zaborowski, M.; Broda, A.; Szmigiel, D. A New Approach for Sensitive Characterization of Semiconductor Laser Beams Using Metal-Semiconductor Thermocouples. *Sensors* **2022**, *22*, 9324. [CrossRef]
7. Wang, J.; Lee, S. Ge-Photodetectors for Si-Based Optoelectronic Integration. *Sensors* **2011**, *11*, 696–718. [CrossRef]
8. Setälä, O.E.; Chen, K.; Pasanen, T.P.; Liu, X.; Radfar, B.; Vähänissi, V.; Savin, H. Boron-Implanted Black Silicon Photodiode with Close-to-Ideal Responsivity from 200 to 1000 nm. *ACS Photonics* **2023**, *10*, 1735–1741. [CrossRef]
9. Sutherland, B.R.; Johnston, A.K.; Ip, A.H.; Xu, J.; Adinolfi, V.; Kanjanaboos, P.; Sargent, E.H. Sensitive, Fast, and Stable Perovskite Photodetectors Exploiting Interface Engineering. *ACS Photonics* **2015**, *2*, 1117–1123. [CrossRef]
10. Tian, M.; Wang, Y.; Zhang, T.; Zhang, C.; Miao, J.; Bian, Z.; Su, X.; Li, Z.; Chai, J.; Wang, A.; et al. Boosting responsivity and speed in 2D material based vertical p-i-n photodiodes with excellent self-powered ability. *Nature Commun.* **2025**, *16*, 5824. [CrossRef] [PubMed]
11. Rogalski, A. Infrared detectors: Status and trends. *Prog. Quantum Electron.* **2003**, *27*, 59–210. [CrossRef]
12. Bao, A.; Lei, C.; Mao, H.; Li, R.; Guan, Y. Study on a High Performance MEMS Infrared Thermopile Detector. *Micromachines* **2019**, *10*, 877. [CrossRef]
13. Lei, C.; Guan, Y.; Liang, T.; Wu, X.; Bai, Y.; Gong, M.; Jia, P.; Xiong, J. Micromachined Infrared Thermopile Detector Based on a Suspended Film Structure. *Photonic Sens.* **2023**, *13*, 230309. [CrossRef]
14. Ahmadzadeh, S.; Gibson, D.; Fleming, L.; Hutson, D.; Song, S.; James, A.; Wells, S.; Forsyth, A.; Bruckshaw, S. Broadband infrared absorber based on a sputter deposited hydrogenated carbon multilayer enhancing MEMS-based CMOS thermopile performance. *Appl. Opt.* **2023**, *62*, B79–B86. [CrossRef]
15. Lei, C.; Zhang, Z.; Shao, B.; Ren, X.; Li, T.; Li, F.; Liang, T. Design and Fabrication of Thermopile Infrared Detector Based on Carbon Black Nanoparticle Absorption Layer. *Photonics* **2025**, *12*, 1016. [CrossRef]
16. Xiang, Z.; Shi, M.; Zhou, N.; Zhang, C.; Ding, X.; Ni, Y.; Chen, D.; Mao, H. A Highly Accurate Method for Measuring Response Time of MEMS Thermopiles. *Micromachines* **2022**, *13*, 1717. [CrossRef] [PubMed]
17. Liu, Z.; Zhang, C.; Ding, X.; Ni, Y.; Zhou, N.; Wang, Y.; Mao, H. A Thermopile-Based Gas Flow Sensor with High Sensitivity for Noninvasive Respiration Monitoring. *Micromachines* **2023**, *14*, 910. [CrossRef] [PubMed]
18. Peng, Y.; Liu, J.; Fu, J.; Luo, Y.; Zhao, X.; Wei, X. Emerging Thermal Detectors Based on Low-Dimensional Materials: Strategies and Progress. *Nanomaterials* **2025**, *15*, 459. [CrossRef] [PubMed]
19. Sun, F.; Shasho, R.T.; Crescimanno, M.; Dawson, N.J. All-Optical Method of Determining Laser Power from the Photomechanical Effect. *Appl. Sci.* **2022**, *12*, 10708. [CrossRef]
20. White, T.J. (Ed.) *Photomechanical Materials, Composites, and Systems: Wireless Transduction of Light into Work*; John Wiley & Sons: Hoboken, NJ, USA, 2017. [CrossRef]
21. Kuzyk, M.G.; Dawson, N.J. Photomechanical materials and applications: A tutorial. *Adv. Opt. Photon.* **2020**, *12*, 847–1011. [CrossRef]
22. Liew, W.H.; Chen, Y.; Alexe, M.; Yao, K. Fast Photostriction in Ferroelectrics. *Small* **2022**, *18*, 2106275. [CrossRef]
23. Boda, M.A.; Chen, C.; He, X.; Yi, Z. Photostriction in emerging inorganic materials for next-generation micro-optomechanical devices. *Appl. Phys. Rev.* **2025**, *12*, 031307. [CrossRef]

24. Uchino, K.; Aizawa, M.; Nomura, L.S. Photostrictive effect in (Pb, La) (Zr, Ti)O_3. *Ferroelectrics* **1985**, *64*, 199–208. [CrossRef]
25. Uchino, K. Micro Walking Machines Using Piezoelectric Actuators. *J. Robot. Mechatron.* **1989**, *1*, 124–127. [CrossRef]
26. Poosanaas, P.; Tonooka, K.; Uchino, K. Photostrictive actuators. *Mechatronics* **2000**, *10*, 467–487. [CrossRef]
27. Koshima, H.; Ojima, N.; Uchimoto, H. Mechanical Motion of Azobenzene Crystals upon Photoirradiation. *J. Am. Chem. Soc.* **2009**, *131*, 6890–6891. [CrossRef] [PubMed]
28. Hao, Y.; Huang, S.; Guo, Y.; Zhou, L.; Hao, H.; Barrett, C.J.; Yu, H. Photoinduced multi-directional deformation of azobenzene molecular crystals. *J. Mater. Chem. C* **2019**, *7*, 503–508. [CrossRef]
29. Yager, K.G.; Tanchak, O.M.; Godbout, C.; Fritzsche, H.; Barrett, C.J. Photomechanical Effects in Azo-Polymers Studied by Neutron Reflectometry. *Macromolecules* **2006**, *39*, 9311–9319. [CrossRef]
30. Wen, H.; Zhang, W.; Weng, Y.; Hu, Z. Photomechanical bending of linear azobenzene polymer. *RSC Adv.* **2014**, *4*, 11776–11781. [CrossRef]
31. Wang, D.H.; Wie, J.J.; Lee, K.M.; White, T.J.; Tan, L.S. Impact of Backbone Rigidity on the Photomechanical Response of Glassy, Azobenzene-Functionalized Polyimides. *Macromolecules* **2014**, *47*, 659–667. [CrossRef]
32. Wie, J.J.; Wang, D.H.; Lee, K.M.; White, T.J.; Tan, L.S. The contribution of hydrogen bonding to the photomechanical response of azobenzene-functionalized polyamides. *J. Mater. Chem. C* **2018**, *6*, 5964–5974. [CrossRef]
33. Zhou, B.; Bernhardt, E.; Bhuyan, A.; Ghorbanishiadeh, Z.; Rasmussen, N.; Lanska, J.; Kuzyk, M.G. Theoretical and experimental studies of photomechanical materials. *J. Opt. Soc. Am. B* **2019**, *36*, 1492–1517. [CrossRef]
34. Ghorbanishiadeh, Z.; Bhuyan, A.; Zhou, B.; Sheibani Karkhaneh, M.; Kuzyk, M.G. Mechanisms of the Photomechanical Response in Thin-Film Dye-Doped Glassy Polymers. *Polymers* **2025**, *17*, 254. [CrossRef]
35. Camacho-Lopez, M.; Finkelmann, H.; Palffy-Muhoray, P.; Shelley, M. Fast liquid-crystal elastomer swims into the dark. *Nature Mater.* **2004**, *3*, 307–310. [CrossRef] [PubMed]
36. Kondo, M.; Miyasato, R.; Naka, Y.; ichi Mamiya, J.; Kinoshita, M.; Yu, Y.; Barrett, C.J.; Ikeda, T. Photomechanical properties of azobenzene liquid-crystalline elastomers. *Liq. Cryst.* **2009**, *36*, 1289–1293. [CrossRef]
37. Sánchez-Ferrer, A.; Merekalov, A.; Finkelmann, H. Opto-Mechanical Effect in Photoactive Nematic Side-Chain Liquid-Crystalline Elastomers. *Macromol. Rapid Commun.* **2011**, *32*, 671–678. [CrossRef] [PubMed]
38. Dawson, N.J.; Kuzyk, M.G.; Neal, J.; Luchette, P.; Palffy-Muhoray, P. Cascading of liquid crystal elastomer photomechanical optical devices. *Opt. Commun.* **2011**, *284*, 991–993. [CrossRef]
39. Svanidze, A.; Kundu, S.; Iadlovska, O.; Thakur, A.K.; Zheng, X.; Palffy-Muhoray, P. The Effects of Network Architecture on the Photomechanical Performance of Azo-Acrylate Liquid Crystal Elastomers. *Crystals* **2025**, *15*, 1. [CrossRef]
40. Cho, E.h.; Luu, K.; Park, S.y. Mechano-Actuated Light-Responsive Main-Chain Liquid Crystal Elastomers. *Macromolecules* **2021**, *54*, 5397–5409. [CrossRef]
41. Dawson, N.J.; Kuzyk, M.G.; Neal, J.; Luchette, P.; Palffy-Muhoray, P. Experimental studies of the mechanisms of photomechanical effects in a nematic liquid crystal elastomer. *J. Opt. Soc. Am. B* **2011**, *28*, 1916–1921. [CrossRef]
42. Dawson, N.J.; Kuzyk, M.G.; Neal, J.; Luchette, P.; Palffy-Muhoray, P. Modeling the mechanisms of the photomechanical response of a nematic liquid crystal elastomer. *J. Opt. Soc. Am. B* **2011**, *28*, 2134–2141. [CrossRef]
43. Pilz da Cunha, M.; van Thoor, E.A.J.; Debije, M.G.; Broer, D.J.; Schenning, A.P.H.J. Unravelling the photothermal and photomechanical contributions to actuation of azobenzene-doped liquid crystal polymers in air and water. *J. Mater. Chem. C* **2019**, *7*, 13502–13509. [CrossRef]
44. Zhang, W.; Nan, Y.; Wu, Z.; Shen, Y.; Luo, D. Photothermal-Driven Liquid Crystal Elastomers: Materials, Alignment and Applications. *Molecules* **2022**, *27*, 4330. [CrossRef]
45. Huang, Y.; Yu, Q.; Su, C.; Jiang, J.; Chen, N.; Shao, H. Light-Responsive Soft Actuators: Mechanism, Materials, Fabrication, and Applications. *Actuators* **2021**, *10*, 298. [CrossRef]
46. Li, S.; Cai, Z.; Han, J.; Ma, Y.; Tong, Z.; Wang, M.; Xiao, L.; Jia, S.; Chen, X. Fast-response photothermal bilayer actuator based on poly(N-isopropylacrylamide)–graphene oxide–hydroxyethyl methacrylate/polydimethylsiloxane. *RSC Adv.* **2023**, *13*, 18090–18098. [CrossRef]
47. Chen, J.; Zhao, X.; Zhao, H. A photothermal soft actuator based on graphene/PDMS composite materials reinforced by carbon fiber skeleton. *AIMS Mater. Sci.* **2025**, *12*, 301–317. [CrossRef]
48. Loomis, J.; King, B.; Burkhead, T.; Xu, P.; Bessler, N.; Terentjev, E.; Panchapakesan, B. Graphene-nanoplatelet-based photomechanical actuators. *Nanotechnology* **2012**, *23*, 045501. [CrossRef] [PubMed]
49. Niu, D.; Jiang, W.; Liu, H.; Zhao, T.; Lei, B.; Li, Y.; Yin, L.; Shi, Y.; Chen, B.; Lu, B. Reversible Bending Behaviors of Photomechanical Soft Actuators Based on Graphene Nanocomposites. *Sci. Rep.* **2016**, *6*, 27366. [CrossRef]
50. Liu, H.; Niu, D.; Jiang, W.; Zhao, T.; Lei, B.; Yin, L.; Shi, Y.; Chen, B.; Lu, B. Illumination-oriented and thickness-dependent photomechanical bilayer actuators realized by graphene-nanoplatelets. *Sens. Actuators A* **2016**, *239*, 45–53. [CrossRef]
51. Knitter, M.; Ferreira, L.; Sheffield, D.R.; Pusateri, J.; Dawson, N.J. Uniaxial photomechanical motion in large diameter polydimethylsiloxane optical fibers with fluoropolymer claddings. *J. Opt. Microsyst.* **2024**, *4*, 013501. [CrossRef]

52. Seoul Semiconductor Inc. *Mid-Power LED—3030 Series*; Seoul Semiconductor Inc.: Ansan, Republic of Korea, 2019.
53. Müller, A.; Wapler, M.C.; Wallrabe, U. A quick and accurate method to determine the Poisson's ratio and the coefficient of thermal expansion of PDMS. *Soft Matter* **2019**, *15*, 779–784. [CrossRef] [PubMed]